Large enhancement of critical-current density due to vortex matching at the periodic facet structure in $YBa_2Cu_3O_{7-\delta}$ bicrystals

X. Y. Cai and A. Gurevich
Applied Superconductivity Center, University of Wisconsin-Madison, Madison, Wisconsin 53706

I-Fei Tsu
Seagate Technology, Bloomington, Minnesota 55435

D. L. Kaiser
Ceramics Division, National Institute of Standard and Technology, Gaithersburg, Maryland 20899

S. E. Babcock and D. C. Larbalestier
Applied Superconductivity Center, University of Wisconsin-Madison, Madison, Wisconsin 53706

(Received 8 September 1997)

We observed pronounced peaks in the critical-current density $J_b(B)$ versus applied magnetic field B in $YBa_2Cu_3O_{7-\delta}$ bicrystals well above the lower critical field. These peaks correspond to the fields for which the spacing between intragrain vortices is commensurate with the wavelength of the periodic grain boundary facet structure observed in the same bicrystals. The peaks were observed on a group of grain boundaries that were isolated from four bulk [001]-tilt bicrystals with misorientation angles around 15°, which lie in the transition region from strong to weak coupling. The matching effect provides direct evidence that faceting strongly modulates the coupling strength of grain boundaries and can substantially increase $J_b(B)$ in high magnetic fields. Periodic modulation of the intergrain coupling by the strain fields observed at the facet junctions by transmission electron microscopy is proposed as the origin of the $J_c(B)$ enhancement.
[S0163-1829(98)07917-X]

I. INTRODUCTION

Since the discovery of high-temperature superconductors (HTS), significant efforts have been devoted to the investigation of the electrical transport through weakly linked grain boundaries that strongly limit the current-carrying capability of HTS materials.[1–3] An important subject that has recently drawn much attention is the evidence of nanoscale (1–100 nm) inhomogeneities of grain boundaries that are observed in HTS bicrystals over the entire misorientation range.[3–5] Analysis of the field dependence of the intergranular critical-current density $J_b(B)$ indicates that it is often spatially nonuniform on the nanoscale, suggesting that grain boundaries should be treated as an array of microbridges or filaments,[6,7] rather than as uniform interfaces. However, the microstructural origin of the J_b heterogeneity has not been identified unambiguously. Grain boundary structures and properties are usually nonuniform on a variety of scales.[8,9] In general, this makes it very difficult to obtain a direct correlation between superconducting properties and the grain boundary nanostructure and microstructure.

One example of the complexity of grain boundary heterogeneity is the hierarchy of facets that has been observed in HTS grain boundaries.[8,10] Boundaries in bulk scale bicrystals of both $YBa_2Cu_3O_7$ and $Bi_2Sr_2CaCu_2O_x$ that appear to be planar in light microscopy studies in fact show a characteristic facet pattern on the $\sim$100 nm length scale and further subfaceting on the nanoscale ($\sim$10 nm) in many cases. There are several mechanisms by which faceting could affect the grain boundary superconductive coupling. For instance, there are long-range strain fields associated with the facet junctions[8] and inhomogeneous copper[11] and hole concentrations,[12,13] which have been shown to vary along the grain boundary approximately in accordance with the facet structure. Recently it was pointed out that faceting could cause a strong modulation of the intergrain critical-current density with the position along the faceted grain boundary as a result of the d-wave symmetry of the superconducting order parameter.[14]

This paper focuses on a combined electromagnetic and microstructural study of bicrystals with well-defined, rather periodic grain boundary facet structure, the average period ranging from 35 to 100 nm. These bicrystals have [001]-tilt character and misorientation angles θ around 15°, close to the critical angle θ_c that characterizes a crossover between strong and weak coupling.[15] Pronounced peaks in $J_b(B)$ were observed for the fields $B \gg B_{c1}$ at which the flux line lattice in the grains is commensurate with the periodic facet structure. This correlation of magnetic and microstructural length scales provides direct evidence that faceting strongly modulates the superconducting coupling across grain boundaries for B well above the lower critical field B_{c1}.

In this paper we present the microstructural and electromagnetic data, followed by a discussion of the general characteristics of the observed peaks in $J_b(B)$. Then we consider different mechanisms that can give rise to the observed high-field peaks. Finally we analyze the specific microstructural origin of the coupling modulation caused by faceting.

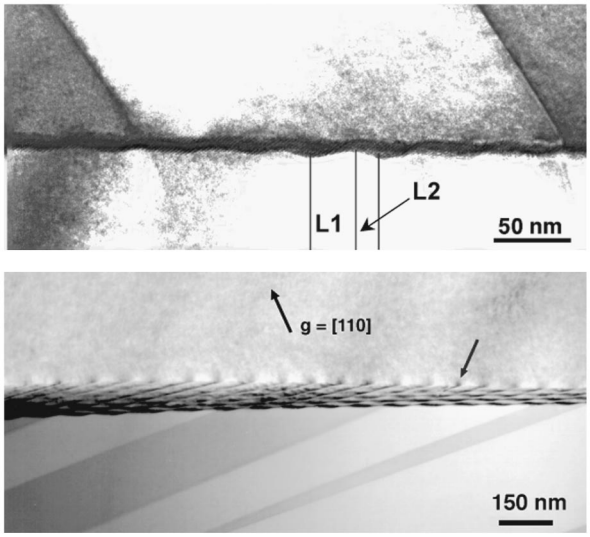

FIG. 1. Diffraction-contrast TEM images of bicrystal *A* obtained with the electron beam nearly along [001], showing the faceted boundary topography (a). The components of the sawtoothed facet structure is mixed, not pure tilt, in this case. Mixed-type facets have been observed in other bicrystals as well, but pure-tilt facets are more common. The facets in bicrystals *B* and *C* were [001] tilt (b) $g//[110]$ two-beam image in which the dislocationlike strain field (contrast) of the facet junctions is apparent. Arrow indicates the orientation of the facet junction dislocations.

II. FACET STRUCTURE OF GRAIN BOUNDARIES IN THE BICRYSTALS

The grain boundaries used in this work were selected from four bulk-scale $YBa_2Cu_3O_{7-\delta}$ (YBCO) bicrystals produced by a flux-growth technique.[16] Typical dimensions of the crystals were 150–250 μm along the *a* and *b* axes, and $\sim$100 μm along the *c* axis. Some sections of the grain boundaries in the as-received bicrystals appeared curved on the scale of light microscope images. In order to begin with better-defined grain boundary sections, the bicrystals were thinned to 10–20 μm along the *c* axis and cut with a precision laser cutter so as to isolate subsections that appeared to be planar with the same boundary normal throughout and of pure [001]-tilt character on the basis of light microscopy investigations.

After electromagnetic measurement, the nanoscale topography and crystallography of the grain boundaries in bicrystals *A*, *B*, and *C* were characterized by transmission electron microscopy (TEM). (We were unsuccessful in preparing a TEM sample from bicrystal *D*.) The nominally θ[001]-type misorientation relationship of the boundaries was confirmed by selected-area electron-diffraction pattern analysis, which gave θ values of 14°, 15°, and 15° and *c*-axis misalignments of 3°, 0.9°, and 2.5° for bicrystals *A*, *B*, and *C*, respectively. TEM imaging revealed a striking feature of the topography of all three boundaries. Sawtoothed facet structures like that shown in Fig. 1 persisted in all regions of the boundaries that were imaged by TEM. The facet structure was rather regular with each period (D_f) comprised of two different facets (L_1 and L_2). TEM images were obtained from several different regions of bicrystal *A* by repeatedly ion milling the sample to create new electron transparent sections. Images of these sections confirmed that the facet period was largely unchanged over a 80-μm-long stretch of the boundary. The periods of all imaged facets of this boundary fell into the range of 30–50 nm. An average period of 40 nm ($L_1 \approx 30$ and $L_2 \approx 10$ nm) was derived from measurements on 40 periods of the facet structure. The average periods D_f of the facet structure were 80 nm ($L_1 \approx 40$, $L_2 \approx 40$ nm) for bicrystal *B*, and 35 nm ($L_1 \approx 20$, $L_2 \approx 15$ nm) for bicrystal *C*, where D_f for bicrystals *B* and *C* was derived from measurements on 12 and 6 facet periods, respectively.

TABLE I. Normal and superconducting parameters of the grain boundaries.

	R_bA (nΩ cm^2)	J_b (0,77 K) (10^3 A/cm^2)	a_0 (B_p) (nm)	D_f (L_1,L_2) (nm)
A	4.5	3.5	45	40 (30,10)
B	4.2	4.0	93	80 (40,40)
C	4.8	3.1	45	35 (20,15)
D	7.5	2.9	176,88	not measured

The two diffraction-contrast TEM images of the boundary in bicrystal *A* shown in Fig. 1 illustrate the additional structural features that were observed in all three bicrystals studied. Figure 1(a), which corresponds to a viewing axis near [001], shows the topography of the faceted boundary. Figure 1(b) shows the same boundary as in Fig. 1(a), but imaged at a $g//\langle 110\rangle$ two-beam condition by tilting the bicrystal $\approx$20° away from the [001] orientation. The facet structure is masked by projection effects at this specimen tilt. However, the image clearly shows the second hallmark feature of the sawtooth facet structures that has been observed in all of these bicrystals, as well as many others.[8,10,11] The dark lines oriented at $\sim$45° to the edge of the micrograph show the image contrast behavior of the facet intersection lines (junctions). The dislocationlike contrast implies that the boundaries are characterized by a longer-range dipole strain field near the facet junctions that is superimposed on the short-range grain boundary dislocation network strain field (of length scale $\sim$1 nm at $\sim$15°). A more detailed description of the microstructures and of general nature of these sawtoothed facet structures is given elsewhere.[8,10]

III. FIELD DEPENDENCE OF $J_b(B)$

The intergrain transport properties were determined using a four-probe method. The current leads were attached to the sides of the crystals parallel to the *c* axis so as to provide relatively uniform current feed into the *ab* planes of the bicrystal. External magnetic field was applied parallel to the *c* axes, and thus parallel to the plane of the grain boundary. The voltage resolution for the measurements of *V*-*I* characteristics was below 10 nV, and the voltage criterion for the intergranular critical current I_b was 100 nV. The dependence of I_b on *B* was measured in both weak (0–20 mT) and strong (0–10 T) fields. The effect of temperature on the $I_b(B)$ behavior was examined for 24 K$<T<$85 K. We also measured the magnetoresistance $R_b(B)=V_b(B)/I$ at constant $I > I_b(B)$ by recording the voltage $V_b(B)$ across current-

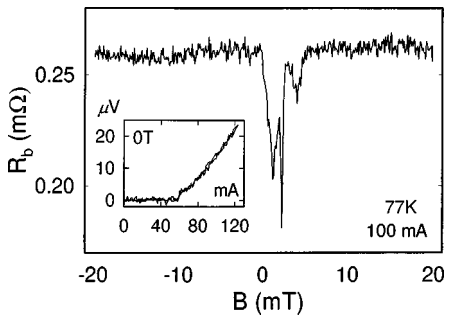

FIG. 2. Magnetoresistance R_b (B, 77 K) of bicrystal A. Inset shows the V-I curve measured at zero field and 77 K.

biased grain boundaries. In all cases we found a good correlation between the $I_b(B)$ peaks and the negative magnetoresistance peaks in $R_b(B)$.

The basic normal and superconducting parameters of these grain boundaries, such as resistivity R_bA, where A is the area of the boundary, and zero-field critical-current density J_b (77 K) are listed in Table I. They were similar for all samples studied, $R_bA=4.5–7.5\ \mathrm{n\Omega\ cm^2}$, and J_b (0,77 K) $=2.9–4.0\ \mathrm{kA/cm^2}$. The magnetoresistance R_b (B,77 K) $=V_b(B)/I$ of bicrystal A at 77 K and the zero-field V-I curve are shown in Fig. 2. The $R_b(B)$ behavior shown in Fig. 2 is typical of all weak-linked bicrystals that we have measured before. Such $R_b(B)$ behavior is consistent with a direct measurement of the $I_b(B)$ behavior for weak-linked grain boundaries, i.e., $I_b(B)$ is depressed by mT fields, tending to a small, nearly field-independent ''residual'' supercurrent at $B>20$ mT.

Extended V-I curves for bicrystal A in the high-field region $5<B<9$ T at 77 K are shown in Fig. 3. This field range includes the irreversibility field B^* (77 K)$\approx$7 T for flux-grown single crystals. At large voltage and currents, all V-I curves for $B\leqslant B^*$ (77 K) exhibit the same Ohmic behavior, which we believe is determined by the grain boundary resistance, indicating that the observed dissipation is restricted to the grain boundary region. For $B>B^*$, an additional intragranular dissipation develops. Thus, even for these crystals with comparatively low intragranular critical-current densities, the overall critical current is limited by the grain boundary. The negative curvature of the low-voltage portions of the V-I curves taken at 5–7 T indicates that a nonzero ''residual'' supercurrent persists up to B^* (77 K).

The most interesting transport behavior of these bicrystals was observed in the field range lying between that of Figs. 2

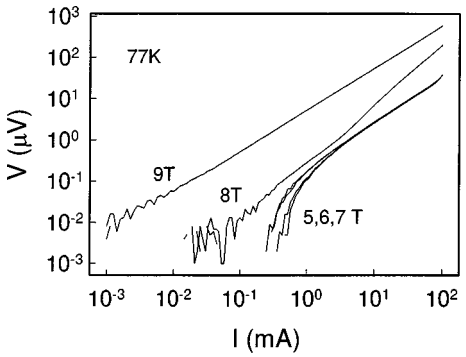

FIG. 3. V-I curves in high field (5–9 T) at 77 K for bicrystal A.

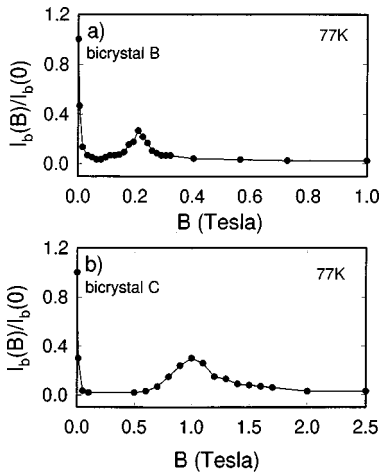

FIG. 4. Normalized $I_b(B,77\ \mathrm{K})/I_b(0,77\ \mathrm{K})$ for bicrystals B (a) and C (b). $J_b(0,77\ \mathrm{K})$ is about $4{,}500\ \mathrm{A/cm^2}$ for both bicrystals. Pronounced peaks at $B_p=0.2$ T (a) and 1 T (b) are shown.

and 3, where all bicrystals exhibited substantial peaks in $I_b(B)$ at $B=B_p$, which varied from 60 mT to 1 T for the different samples (see Table I). The major characteristics of this effect are summarized in Figs. 4–6. Figures 4(a) and 4(b) show normalized critical current $I_b(B)/I_b(0)$ for bicrystals B and C. The peak in $I_b(B)$ at $B=B_p$ is quite pronounced, being about 20–30 times larger than the ''residual'' supercurrent and reaching 20–30% of the zero-field I_b. For bicrystal C, the intergrain J_b ($B_p=1$ T, 77 K) reached about 50% of the single crystal J_c (1 T, 77 K) value.

Figures 5(a) and 5(b) show the $R_b(B)$ curves recorded on bicrystal D at 77 and 64 K. In this case, two negative magnetoresistance peaks at B_{p1} and B_{p2} are visible for both temperatures, with $B_{p2}\approx(4\pm0.5)B_{p1}$. These $R_b(B)$ curves exhibit hysteresis, which rapidly decreases as the field increases. This may account for the absence of any apparent hysteresis in the $I_b(B)$ curves of bicrystals B and C in Fig. 4, for which the peaks in $I_b(B)$ occur at much higher fields (1 and 0.2 T). It is interesting that the hysteresis effect in these bulk bicrystals occurs at much lower fields than for thin film bicrystals, where hysteresis at fields up to 8 T has been reported.[5]

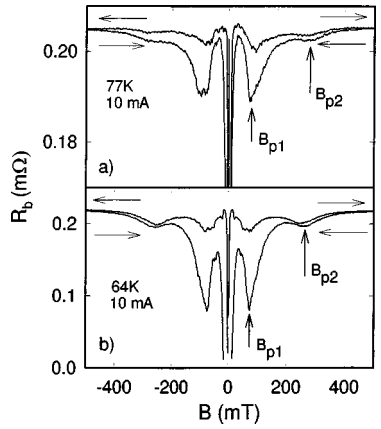

FIG. 5. Magnetoresistance $R_b(B)$ data for bicrystal D at 77 K (a) and 64 K (b) showing dips at $B=B_{p1}$ and $B=B_{p2}$, $B_{p2}\approx4B_{p1}$. B_{p1} and B_{p2} values are the same for 77 and 64 K.

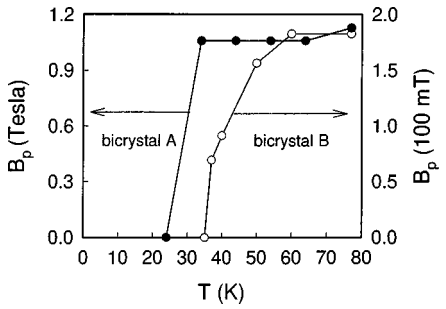

FIG. 6. Temperature dependences of the $I_b(B)$ peak position B_p for bicrystals A (●) and B (○).

The temperature dependence of the $I_b(B)$ peaks for bicrystals A and B, shown in Fig. 6, was determined by measuring the positions B_p of the negative magnetoresistance peaks from 77 K down to 25 K. For bicrystals A and B, B_p was found to be essentially temperature independent above a temperature T_0, where $T_0 \approx 32$ K for A and $T_0 \approx 60$ K for B. A similar result was also obtained for bicrystal D, as evidenced by the B_{p1} and B_{p2} values measured at the two different temperatures [Figs. 5(a) and 5(b)]. Below its T_0 of 30 K, the $I_b(B)$ peak of bicrystal A rapidly decreased and disappeared by ≈ 25 K, whereas the $I_b(B)$ peak of bicrystal B gradually shrank below its T_0 of 60 K and shifted to lower temperatures, finally disappearing by ≈ 35 K.

The weak-field $I_b(B)$ behavior, as reflected in the $R_b(B)$ curve shown in Fig. 2, clearly indicates an overall reduced coupling at these 15° [001]-tilt grain boundaries. For thin-film grain boundaries, the macroscopic average coupling strength is usually characterized by the zero-field critical-current density $J_b(0)$, or by the ratio $J_b(0)/J_c(0)$. This method is less justifiable for bulk bicrystals because $J_b(0)$ is limited by significant self-field effects.[17] As a result, the values of J_b (77 K, 0 T), which are listed in Table I for comparison between different samples with similar dimensions, cannot be considered as a measure of the intrinsic J_b. In a separate experiment, we found that the zero-field J_b (77 K) of a bicrystal was increased by a factor of 6 when its thickness was reduced from 100 to 30 μm, consistent with a substantial self-field effect. We note that the measured boundary resistivity $R_b A \approx 5\ \mathrm{n\Omega\ cm^2}$ is comparable to the lowest reported values for weak-linked thin-film bicrystals.[18] Thus, there is no reason to conclude that these bulk bicrystals have poorer grain boundary properties than those of thin-film bicrystals.

A key aspect of these results is that the observed peaks in $I_b(B)$ are temperature independent over a large temperature range and occur at fields $B = B_p$ for which the intervortex spacing $a_0(B_p) = 1.07(\Phi_0/H)^{1/2}$ is commensurate with the average period of the facet structure, D_f. The values of $a_0(B_p)$ and D_f for bicrystals A, B, and C are shown in Table I. There is a good correlation between $a_0(B_p)$ and D_f for each of these bicrystals: D_f differs from $a_0(B_p)$ by 6% for A, by 20% for B, and by 27% for C. The greater differences between D_f and $a_0(B_p)$ for bicrystals B and C may be the experimental uncertainty of D_f due to the smaller number of facet units used in the calculation of the average period.

In addition to the $I_b(B)$-peak behavior, all of the bicrystals showed a field-independent ''residual'' supercurrent that persisted up to magnetic fields close to the intragrain $B_g^*(77\ \mathrm{K})$. This ''residual'' supercurrent is commonly observed in HTS grain boundaries, and has been attributed to structural disorder along grain boundaries,[19] such as that resulting from oxygen defects[7] or the dislocation networks.[6] Because of the quasiperiodic character of the facet structure in these grain boundaries, the distribution of oxygen defects and hole concentration in these grain boundaries is likely to be periodic too. This supposition is strongly supported by the temperature effect on the $I_c(B)$ peaks as discussed later. The intergrain irreversibility field $B_b^*(77\ \mathrm{K})$ remains close to the $B_g^*(77\ \mathrm{K})$, indicating that these grain boundaries contain paths that can transmit supercurrent up to at least the irreversibility field of the grains themselves.

IV. DISCUSSION

The observed correlation between $a_0(B_p)$ and D_f indicates that the facet structure strongly modulates the local intergrain $J_b(x)$. Generally, the overall intergrain critical current density $J_b = I_b/A$ is determined by the pinning force $f = f_1 + f_2$ of the vortices at the grain boundary (intergrain vortices). Here f_1 is due to the interaction of intergrain vortices with the inhomogeneities of the grain boundary caused by the facet structure, while f_2 comes from the magnetic interaction of the intergrain vortices with the pinned intragrain vortices.[20] In the transition region from strong to weak coupling, the nature of the intergrain vortices and their interactions with facet structure and intragrain vortices strongly depends on θ. In the dislocation model of the grain boundary, the description of the $J_b(B)$ behavior is different for $\theta > \theta_c$ and $\theta < \theta_c$.[21] For $\theta > \theta_c$, i.e., the weak-coupling limit, the grain boundary is often regarded as a continuous interface formed by overlapping dislocation cores that are generally assumed to be in an insulating state.[21,22] Such a high-angle grain boundary can be modeled as a parallel array of decoupled Josephson contacts formed by the grain boundary facets, and the peaks in $J_b(B)$ are due to Fraunhofer oscillations modified by the presence of the intragrain Abrikosov vortices (A vortices) at fields well above B_{c1}. For $\theta < \theta_c$, the dislocation cores do not overlap and the grain boundary contains high critical-current density channels.[15,21] In this case the intergrain vortices are mixed Abrikosov vortices with phase-Josephson cores (AJ vortices),[23] unlike the usual Josephson vortices (J vortices) for $\theta > \theta_c$. The facet structure provides a periodic pinning potential for the intergrain AJ vortices, resulting in enhancement of J_b, if the intervortex spacing is commensurate with D_f. Interestingly, both scenarios for $\theta > \theta_c$ and $\theta < \theta_c$ yield qualitatively similar peaks in $J_b(B)$. In the following we consider the cases $\theta > \theta_c$ and $\theta < \theta_c$ separately.

A. Fraunhofer oscillations at $\theta > \theta_c$

This case corresponds to a weak coupling condition $J_b \ll J_c$ where J_c is the intragrain critical-current density. The observed J_b is determined by the transparency of the grain boundary to the supercurrent, while the intragrain vortices are assumed to be fixed by strong bulk pinning and thus unaffected by the weak Josephson current flowing through the grain boundary. However, the intragrain A vortices

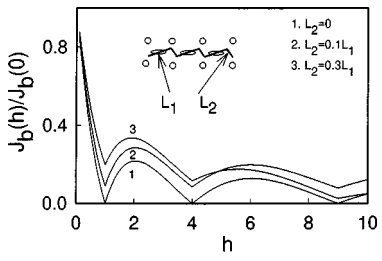

FIG. 7. Normalized critical current $J_b(h)/J_b(0)$ as a function of the reduced field $h=B(\zeta L_1)^2/\phi_0$ calculated from Eq. (5) for $J_1=J_2=J_b$ and different L_1/L_2 ratios. The inset shows the model geometry of a parallel array of decoupled Josephson contacts at $B\approx B_p$; circles and ellipses represent the intragrain and intergrain vortices, respectively.

strongly influence the field dependence of $J_b(B)$ through changing the distribution of magnetization currents around the grain boundary. We model the grain boundary as an array of parallel decoupled uniform junctions of length $L\approx D_f$; the observed $I_b(B)$ peaks thus correspond to a modified Fraunhofer pattern of a short Josephson contact in the presence of intragrain vortices. The field dependence of $J_b(B)$ of such a contact is given by[24]

$$J_b(B)=J_0[\phi_0/(\pi BL\Lambda_0)]\left|\sin(\pi BL\Lambda_0/\phi_0)\right|, \qquad (1)$$

where $\Lambda_0(B)$ is the grain boundary magnetic thickness, which may be much larger than the structural thickness d, ϕ_0 is the flux quantum, and J_0 is the tunneling Josephson current at $B=0$. For $B<B_{c1}$, the magnetic thickness of the contact, $\Lambda_0(B)=d+2\lambda$, is determined by the Meissner screening currents flowing parallel to the grain boundary, where λ is the London penetration depth. In this case, Eq. (1) gives the well-known Fraunhofer dependence of $J_b(B)$. For $B>B_{c1}$, penetration of vortices into the grains strongly affects the magnetization currents flowing parallel to the grain boundary, and $\Lambda_0(B)$ becomes of the order of the intervortex spacing,[25]

$$\Lambda_0=z_0-\frac{a_0}{2}-8\pi\lambda\,\frac{M}{B}, \qquad (2)$$

where $M=(\phi_0/32\pi^2\lambda^2)\ln(B_0/B)$ is the equilibrium magnetization, B_0 is of the order of the upper critical field B_{c2}, and z_0 is the distance of the first vortex row from the grain boundary.[26] For $B\gg B_{c1}$, the last term in Eq. (2) can be neglected; thus $\Lambda_0(B)=\zeta a_0=\zeta(\phi_0/B)^{1/2}$, where ζ is a number of order unity, which generally depends on bulk pinning and the geometry of the grain boundary. For our bicrystals, bulk pinning is comparatively weak, so ζ is mostly determined by the geometry of the facet structure. Substituting $\Lambda_0(B)=\zeta(\phi_0/B)^{1/2}$ into Eq. (1), we arrive at

$$J_b(B)=(J_0/\pi\zeta L)(\phi_0/B)^{1/2}\left|\sin[\pi\zeta L(B/\phi_0)^{1/2}]\right|. \qquad (3)$$

Figure 7 shows the normalized current density $J_b(h)/J_0$ as a function of the dimensionless field $h=B(\zeta L)^2/\phi_0$ calculated from Eq. (3) (curve 1). Here $J_b(h)/J_0$ vanishes at $h=n^2$ [or $B=\phi_0 n^2/(\zeta L)^2$], and the positions of the maxima of $J_b(h)/J_0$ increases quadratically with n at large n, where $n=0,1,2,\ldots$. The first peak in $J_b(h)$ at $h\approx 2.2$ [$B_p\approx 2.2\phi_0/(\zeta L)^2$] is about 20% of J_0, in agreement with the observed height of the first peak [$J_b(B_p)/J_0\approx 0.2-0.3$]. The higher-order commensurate peaks in $J_b(B)$ lie in the field region where $J_b(B)$ drops below the noise level. However, the magnetoresistance measurements shown in Fig. 5 clearly revealed a satellite peak in $R_b(B)$ located at $B_{p2}\approx 4B_{p1}$, in accordance with Eq. (3). The observed matching condition ($a_0\approx L$) for the first peak in $J_b(B)$ requires $\zeta\approx 1.35$.

If the facet lengths have a distribution function $F(L)$, the averaged $J_b(B)$ becomes[27]

$$J_b(B)=J_0L_0\int_0^\infty F(L)\left|\sin\frac{L}{L_0}\right|\frac{dL}{L}, \qquad (4)$$

where $L_0=(\phi_0/B)^{1/2}/\pi\zeta\sim a_0$. The distribution of L decreases the amplitude of higher-order peaks in $J_b(B)$ and smears out the cusps in $J_b(B)$, producing minima which have finite $J_b(B)$. For instance, if the grain boundary can be modeled as alternating segments of length L_1 and L_2 with local average critical current densities J_1 and J_2, then

$$J_b(B)=\frac{1}{\zeta\pi(L_1+L_2)}\left[J_1\left|\sin\,\pi\zeta L_1\sqrt{\frac{B}{\phi_0}}\right|+J_2\left|\sin\,\pi\zeta L_2\sqrt{\frac{B}{\phi_0}}\right|\right]\sqrt{\frac{\phi_0}{B}}. \qquad (5)$$

This model may be more adequate to describe the $J_b(B)$ dependence of a faceted grain boundary, since the lengths of the grain boundary segments that form the sawtooth facet structure in Fig. 1 can be unequal as was mentioned before. Figure 7 shows the dependence $J_b(h)/J_0$ as a function of the reduced field $h=B(\zeta L_1)^2/\phi_0$ for different L_1/L_2 and $J_1=J_2=J_0$. This simple model gives a qualitative description of the observed matching effect, although the measured shape of the $I_b(B)$ peaks may substantially deviate from that given by Eq. (3). In particular, the calculated peak was about three times broader than that observed in Fig. 4(b), which can hardly be ascribed to a distribution of the facet lengths D_f, or to nonuniform current flow through the junction, which usually broadens the Fraunhofer peaks. There are several factors that can influence the shape of the $I_b(B)$ peak. For example, parallel electron-energy-loss spectroscopy data obtained on similar bicrystal grain boundaries indicated that the grain boundary is sheathed by an hole-depleted region with the thickness ≈ 40 nm,[28] comparable to the magnetic thickness $\Lambda_0\approx a_0$ of the grain boundary. This layer of reduced T_c can affect the position z_0 of the first vortex row neighboring the grain boundary, which plays a key role in the field dependence of $J_b(B)$ at $B\gg B_{c1}$. Furthermore, the peak $J_b(B_p)$ value was found to be only two times smaller than the intragrain $J_c(B)$ measured on a similar single crystal. The small $J_c(B)$ may violate the applicability condition $J_b(B)\ll J_c(B)$ of Eq. (3), which implies fixed intragrain vortices unaffected by the weak Josephson current through the grain boundary. For $J_b(B)\sim J_c(B)$, the commensurate facet structure gives rise to an additional pinning of bulk vortices, thus changing their arrangement near the grain boundary and making ζ dependent on B.

The substantial hysteresis in the magnetoresistance $R_b(B)$ in Fig. 5 can be due to the hysteretic field distribution in the grains described by the Bean model.[30] Indeed, as the applied

field B_a increases, the local field $B(x)$ along the grain boundary varies from $B_a - B_g$ in the center to B_a at the sample edge, where B_g is the field of full flux penetration in the grains. As B_a decreases, the local field $B(x)$ varies from $B_a + B_g$ in the center to B_a at the sample edge. The field variation along the boundary produces a mismatch between the local intervortex spacing $a_0(B)$ and the periodic facet structure, thus suppressing the commensurate peaks in $J_b(B)$. The suppression of the peaks in $J_b(B_a)$ is stronger in the case of increasing B_a, for which the local $B(x)$ is smaller than B_a, and $a_0 = [\phi_0/B(x)]^{1/2}$ is more inhomogeneous as compared to the case of decreasing B_a, for which $B(x) > B_a$. In this model, the hysteresis of $J_b(B)$ is most pronounced in the low-field region, in qualitative accordance with the observed hysteretic $R_b(B)$ curves in Fig. 5. A more quantitative description is complicated by the high aspect ratio ($\approx 10-20$) of our thin bicrystals, which were measured at perpendicular magnetic field and by the strong dependence of $J_c(B)$ at low B. For this geometry, both the magneto-optical imaging and detailed calculations of the local flux distribution[31,32] have revealed very inhomogeneous $B(\mathbf{r})$ in the bulk and nonmonotonic $B(x)$ profiles along the grain boundaries due to strong demagnetizing effects. Likewise, to the parallel field orientation, both the $B(x)$ along the boundary and the local intervortex spacing $a_0(B)$ for the perpendicular geometry were found to be more inhomogeneous for increasing B_a than those for decreasing B_a, especially for $B_a \sim B_g$.[31,32] This manifests itself in the hysteretic $R_b(B)$ and the suppression of the commensurate peaks in the low-field region.

B. Commensurate pinning at $\theta < \theta_c$

For $\theta < \theta_c$, the dislocation cores do not overlap, thus the grain boundary contains channels of comparatively undisturbed lattice that are able to carry significant supercurrents. The channels strongly affect the structure of the intergrain vortices that turn into intermediate AJ vortices with phase Josephson cores whose length along the grain boundary $1 \approx \xi J_d/J_b$ is larger than the coherence length ξ, where $J_d = c\phi_0/16\pi^2\lambda^2\xi$ is the depairing current density and J_b is the intergrain critical-current density averaged along the grain boundary.[23] Since the AJ vortices have larger core sizes than the A vortices, they are pinned more weakly than the intragrain vortices, thus yielding a smaller intergrain J_b as compared to the intragrain J_c, as is shown in the bicrystals of this study. On the other hand, if $1 < \lambda$, the magnetic interaction between intergrain AJ and intragrain A vortices becomes rather insensitive to the vortex core structure and remains approximately the same as in the bulk. Therefore, the intergrain AJ vortices are maintained with a spacing of $a_0 = (\phi_0/B)^{1/2}$ and $J_b(B)$ is enhanced at fields that satisfy the commensurability condition of $na_0(B) = mD_f$.

The above interpretation of the peaks in $J_b(B)$ is in a sense similar to that of the case $\theta > \theta_c$, since the Fraunhofer $J_b(B)$ patterns can also be interpreted as being due to pinning of Josephson (J) vortices by the junction edges, the peaks in $J_b(B)$ approximately corresponding to half-integer numbers of J vortices in the contact.[29] For periodically modulated long Josephson contacts, similar peaks in $J_b(B)$ can occur due to commensurability of the J vortex structure and the pinning potential.[32,33] However, there is an important difference between the cases $\theta < \theta_c$ and $\theta > \theta_c$, which can be tested experimentally. Indeed, for $\theta > \theta_c$, the grain boundary is a weak link whose $J_b(B)$ is much smaller than the intragrain $J_c(B)$; thus $J_b(B)$ is rather insensitive to the pinning of intragrain A vortices. By contrast, for $\theta < \theta_c$, there is a weakly pinned chain of AJ vortices in the grain boundary that can strongly interact with the intragrain A vortices. This makes $J_b(B)$ dependent not only on the properties of the grain boundary, but also on collective pinning of the intragrain vortex structure near the grain boundary. This can be shown by estimating $J_b(B)$ for an AJ vortex chain moving through a strongly pinned bulk vortex structure.[20]

We consider the case of negligible core pinning of the AJ vortices ($1 \gg \xi$), for which the pinning energy results from quasiperiodic modulations of the magnetic energy $W = -\phi_0 H(\mathbf{r})/4\pi$ of an AJ vortex due to variations $\delta H(\mathbf{r})$ of the local magnetic field $H(\mathbf{r})$ caused by a fixed intragrain vortex structure. The pinning force per unit length is then of the order of $\delta W/a_0$, where $\delta W \sim \phi_0 \delta H/4\pi$ is the amplitude of the fluctuations in $W(\mathbf{r})$, and $\delta H \sim (\phi_0/4\pi\lambda^2)e^{-2\pi}$ at $H \gg H_{c1}$.[26] This gives the critical-current density $J_b \sim c\,\delta H/4\pi a_0$ in the form

$$J_b \cong 0.01 J_d \sqrt{H/H_{c2}}. \tag{6}$$

For YBCO ($\xi = 20$ Å, $\lambda = 2000$ Å, and $J_d \sim 10^8$ A/cm^2), Eq. (6) yields $J_b \sim 10^{-3} J_d \sim 10^5$ A/cm^2 at $B \sim 0.01 B_{c2}$. This calculated J_b value is much larger than the J_c values typically measured in flux-grown YBCO crystals, suggesting that depinning of the AJ intragrain vortices cannot occur independently of the surrounding A vortices. Therefore the observed J_b of low-angle grain boundaries with $\theta < \theta_c$ is due to *collective* pinning of both inter and intragrain vortices.

In the collective pinning model[34] J_b is determined by all vortices lying in a sheet of width R_{cb} near the grain boundary, where R_{cb} is the transverse pinning correlation length determined by both the stronger intragrain pinning and the weaker core pinning of the grain boundary. The R_{cb} is therefore larger than the bulk correlation length R_c far from the grain boundary, and is much larger than the intervortex spacing for the weak bulk pinning typical of our samples. In this case the pinning correlation volume for the grain boundary contains many intragrain A vortices, thus J_b essentially depends on bulk pinning, and should *increase* as the intragrain J_c is increased.

Summarizing these arguments, we expect that $J_b(B)$ is much smaller than $J_c(B)$ and is independent of J_c for high-angle grain boundaries ($\theta > \theta_c$). By contrast, for low-angle grain boundaries ($\theta < \theta_c$), $J_b(B)$ is comparable to $J_c(B)$ and increases as the intragrain $J_c(B)$ is increased.

C. Coupling modulation by the facet structure

Our experimental data show that the magnitude of the peaks in $I_b(B)$ rapidly diminishes as the temperature is lowered below 60 K, thus suggesting that the neighboring facets become coupled at lower temperatures. The facet decoupling at high temperature may result from the long-range strains concentrating near the facet junctions (see Fig. 1), which cause local variations of the critical temperature $T_c(\mathbf{r})$. For small in-plane deformations,[35]

$$T_c(x,y) = T_{c0} - C_a\varepsilon_{aa} - C_b\varepsilon_{bb}. \quad (7)$$

Here $\varepsilon_{aa}(\mathbf{r})$ and $\varepsilon_{bb}(\mathbf{r})$ are the principal values of the strain tensor $\varepsilon_{ik}(\mathbf{r})$ along the a and b axes, T_{c0} corresponds to the undeformed sample, and the constants $C_a = -\partial T_c/\partial\varepsilon_{aa}$ and $C_b = -\partial T_c/\partial\varepsilon_{bb}$ determine the change of T_c under uniaxial deformation. For optimally oxygen-doped $YBa_2Cu_3O_{7-\delta}$ single crystals, pressure experiments have shown that $C_a \approx -200$ K and $C_b \approx 300$ K have opposite signs due to the influence of the Cu-O chains, and the values C_a and C_b can increase by 2–10 times in underdoped samples.[35,36] Rough estimation of strains around the facet structures seen in Fig. 1 have shown that the principal values $\varepsilon_{aa}(\mathbf{r})$ and $\varepsilon_{bb}(\mathbf{r})$ may reach about 1%, even 20 nm away from the facet junctions.[8] According to Eq. (7), these strains can give rise to significant (~ 10 K) local suppression of $T_c(\mathbf{r})$ around the facet junctions on a scale much larger than the coherence length, $\xi \sim 2$ nm, and cause inhomogeneities in the local $J_b(x)$ values along the grain boundary. In addition, the hole depletion measured near grain boundaries[28] may considerably enhance the effect of the strain-induced T_c suppression due to the increase of the constants C_a and C_b.[36] Since the local T_c around the facet junctions is suppressed to a value $T_{c\,\min}$ on a length scale much larger than ξ, or the proximity length $\xi_N = \eta v_F/2\pi T \sim \xi$ at $T \approx T_c$, the strain mechanism provides facet decoupling in the temperature region $T_{c\,\min} < T < T_{c0}$.

An additional contribution to the local T_c suppression can also result from the redistribution of oxygen vacancies in the strained region around the facet junctions.[36] At thermodynamic equilibrium, the concentration $c(\mathbf{r})$ of the vacancies is given by

$$c(r) = c_0 \exp\left(-\frac{K\varepsilon(r)\Omega_0}{T}\right), \quad (8)$$

where K is the bulk elastic modulus, $\varepsilon = \varepsilon_{aa} + \varepsilon_{bb}$ is the local dilatation, Ω_0 is the atomic volume of an oxygen vacancy, and c_0 is the concentration of oxygen vacancies in undeformed samples. Since the redistribution of oxygen vacancies is determined by slow oxygen diffusion, it mostly occurs during bicrystal preparation at temperatures much higher than T_{c0}. As a result, cooling the bicrystal can produce quenched structures of vacancies or other impurities around the grain boundary with nonequilibrium distributions $c(\mathbf{r})$ quite different from those given by Eq. (8). Modulation of the local oxygen concentration by the strains near faceted grain boundaries may result in the filamentary structure proposed by Moeckley *et al.*,[7] who assumed that point contacts, which have dimensions from ≈ 1 to 60 nm, are formed by local clustering of oxygen defects.

Other sources of chemical nonstoichiometry associated with the facet structure are also possible. For example, detailed STEM-EDS studies have shown that excess copper segregates at boundaries in intervals consistent with the periods of the extended strain fields.[11]

IV. CONCLUDING REMARKS

We have studied a group of grain boundaries of flux-growth YBCO [001]-tilt bicrystals with misorientation angles around 15°. These grain boundaries appear planar in light micrographs but are characterized by periodic facet structures on the nanoscale. Transport and microstructural studies showed a pronounced matching effect that manifested itself in distinctive peaks in $I_b(B)$ when the intervortex spacing was commensurate with the period of the facet structure. This observation provides direct evidence that facet structures modulate the order parameter of the grain boundary. Microstructural observation and the temperature dependence of the matching effect suggest that the heterogeneity is controlled by the long-range strain fields that are associated with the facet structure.

The pronounced peak in $J_b(B)$ at high fields correlated with the facet structure offers the possibility that the high-field J_b value of polycrystalline HTS could be substantially enhanced by introducing pinning centers in the intergram and/or intragrain regions.

ACKNOWLEDGMENTS

This work was supported by the NSF Materials Research Group (Grant No. DMR 9214707) and the MRSEC Program (Grant No. DMR 9632527).

[1] D. Dimos, P. Chaudhari, and J. Mannhart, Phys. Rev. B **41**, 4038 (1990).
[2] S. E. Babcock, X. Y. Cai, D. L. Kaiser, and D. C. Larbalestier, Nature (London) **347**, 167 (1990).
[3] S. E. Babcock and J. L. Vargas, Annu. Rev. Mater. Sci. **25**, 193 (1995).
[4] R. Gross, in *Interfaces in Superconducting Systems*, edited by S. L. Shinde and D. Rudman (Springer, New York, 1992), p. 176.
[5] M. Daumling, E. Sarnelli, P. Chaudhari, A. Gupta, and J. Lacey, Appl. Phys. Lett. **61**, 1355 (1992).
[6] E. Sarnelli, P. Chaudhari, and J. Lacey, Appl. Phys. Lett. **62**, 777 (1993).
[7] B. H. Moeckley, D. K. Lathrop, and R. A. Buhrman, Phys. Rev. B **47**, 400 (1993).
[8] I-Fei Tsu, S. E. Babcock, and D. L. Kaiser, J. Mater. Res. **11**, 1383 (1996).
[9] O. M. Froehlich, H. Schulze, A. Beck, B. Mayer, L. Alff, R. Gross, and R. P. Heubener, Appl. Phys. Lett. **66**, 2289 (1995).
[10] I. F. Tsu, J. L. Wang, D. L. Kaiser, and S. E. Babcock (unpublished).
[11] J. L. Vargas, Na Zhang, D. L. Kaiser, and S. E. Babcock (unpublished).
[12] Y. M. Zhu, Y. I. Corcoran, and M. Suenaga, Interface Sci. **1**, 359 (1994).
[13] N. D. Browning, M. F. Chisholm, S. J. Pennycook, D. P. Norton, and D. H. Lowndes, Physica C **212**, 185 (1993).
[14] H. Hilgenkamp, J. Mannhart, and B. Mayer, Phys. Rev. B **53**, 14 586 (1996).
[15] M. F. Chisholm and S. J. Pennycook, Nature (London) **351**, 47 (1991).
[16] D. L. Kaiser, F. Holtzberg, B. Scott, and T. R. McGuire, Appl. Phys. Lett. **51**, 1040 (1987).

[17] M. Tinkham, *Introduction to Superconductivity* (Krieger, Malabar, Florida, 1975), p. 201.
[18] K. Char, M. S. Colclough, L. P. Lee, and G. Zaharchuk, Appl. Phys. Lett. **59**, 2177 (1991).
[19] I. K. Yanson, Zh. Eksp. Teor. Fiz. **58**, 1497 (1970) [Sov. Phys. JETP **31**, 800 (1970)].
[20] A. Gurevich and L. D. Cooley, Phys. Rev. B **50**, 13 563 (1994).
[21] N. F. Heinig, R. D. Redwing, I-Fei Tsu, A. Gurevich, J. E. Nordman, S. E. Babcock, and D. C. Larbalestier, Appl. Phys. Lett. **69**, 577 (1996).
[22] Y. Gao, K. L. Merkle, G. Bai, H. Chang, and D. J. Lam, Physica C **174**, 110 (1991).
[23] A. Gurevich, Phys. Rev. B **46**, 3187 (1992); **48**, 12 857 (1993).
[24] L. N. Bulaevskii, J. R. Clem, L. I. Glazman, and A. P. Malozemoff, Phys. Rev. B **45**, 2545 (1992).
[25] M. V. Fistul' and G. F. Giuliani, Phys. Rev. B **51**, 1090 (1995).
[26] F. F. Ternovskii and L. L. Shekhata, Zh. Eksp. Teor. Fiz. **62**, 2297 (1972) [Sov. Phys. JETP **35**, 1202 (1972)]; A. E. Koshelev, Physica C **223**, 2761 (1994).
[27] R. L. Peterson and J. E. Ekin, Phys. Rev. B **37**, 9848 (1988).
[28] S. E. Babcock, X. Y. Cai, D. C. Larbalestier, D. H. Shin, N. Zhang, H. Zhang, D. L. Kaiser, and Y. Gao, Physica C **227**, 183 (1994).
[29] A. Barone and G. Paterno, *Physics and Applications of the Josephson Effect* (Wiley, New York, 1982).
[30] A. A. Polyanskii, A. Gurevich, A. E. Pashitski, N. F. Heinig, R. D. Redwing, J. E. Nordman, and D. C. Larbalestier, Phys. Rev. B **53**, 8687 (1996).
[31] E. H. Brandt, Phys. Rev. B **54**, 4246 (1996).
[32] R. Fehrenbacher, V. B. Geshkenbein, and G. Blatter, Phys. Rev. B **45**, 5450 (1992).
[33] M. A. Itzler and M. Tinkham, Phys. Rev. B **51**, 435 (1995).
[34] G. Blatter, M. V. Feigelman, V. B. Geshkenbein, A. I. Larkin, and V. M. Vinokur, Rev. Mod. Phys. **66**, 1125 (1994).
[35] H. Takahashi and N. Mori, in *Studies of High Temperature Superconductors*, edited by A. V. Narlikar (Nova Science, New York, 1995), Vol. 16, p. 1.
[36] A. Gurevich and E. A. Pashitskii, Phys. Rev. B **56**, 6213 (1997).